


## Article

# Particle Stimulated Nucleation Effect for Al-Mg-Zr-Sc Alloys with Ni Addition during Multidirectional Forging

Mikhail S. Kishchik<sup>1</sup>, Andrey G. Mochugovskiy<sup>1</sup> , Maxence Cuda<sup>2</sup>, Anna A. Kishchik<sup>1</sup> and Anastasia V. Mikhaylovskaya<sup>1,\*</sup>

<sup>1</sup> Department of Physical Metallurgy of Non-Ferrous Metals, National University of Science and Technology “MISIS”, Leninsky Prospekt 4, 119049 Moscow, Russia; mochugovskiy.ag@misis.ru (A.G.M.); kishchik.aa@misis.ru (A.A.K.)

<sup>2</sup> National School of Engineers of Saint-Étienne, University of Saint-Étienne, 58, Rue Jean Parot, 42023 Saint-Étienne, France; maxence.cuda@gmail.com

\* Correspondence: mikhaylovskaya@misis.ru; Tel.: +7-495-683-4480

**Abstract:** The study aims to investigate the influence of fraction of coarse undeformed particles on the microstructure evolution and mechanical properties of alloys processed by isothermal multidirectional forging (MDF). For this purpose, Al-Mg-Ni-Sc-Zr-based alloys with different Ni concentrations and a fraction of Al<sub>3</sub>Ni particles of solidification origin phase were subjected to MDF at 350 °C. Precipitates of the L1<sub>2</sub>-structured Al<sub>3</sub>(Sc,Zr) phase retained their structure, morphology, and size after MDF and were coherent with the aluminum matrix. The Al<sub>3</sub>Ni phase particles stimulated the nucleation of recrystallized grains and contributed significantly to the formation of an ultrafine-grained structure. The uniformity of the grain structure increased, and the average grain size decreased with an increase in the fraction of Al<sub>3</sub>Ni particles. A fine-grained structure with a mean grain size of 2.4–3.4 μm was observed after MDF with a cumulative strain of 12. The results demonstrate that a bimodal particles size distribution with a volume fraction of nanoscale  $f \sim 0.1\%$  and microscale  $f \sim 8\%$  particles provided for the formation of a homogenous fine-grained structure after MDF and improved the mechanical properties.

**Keywords:** aluminum alloy; particle stimulated nucleation; multidirectional forging; grain refinement; microstructure evolution; mechanical properties



**Citation:** Kishchik, M.S.; Mochugovskiy, A.G.; Cuda, M.; Kishchik, A.A.; Mikhaylovskaya, A.V. Particle Stimulated Nucleation Effect for Al-Mg-Zr-Sc Alloys with Ni Addition during Multidirectional Forging. *Metals* **2023**, *13*, 1499. <https://doi.org/10.3390/met13081499>

Academic Editor: Joan-Josep Suñol

Received: 12 July 2023

Revised: 15 August 2023

Accepted: 17 August 2023

Published: 21 August 2023



**Copyright:** © 2023 by the authors. Licensee MDPI, Basel, Switzerland. This article is an open access article distributed under the terms and conditions of the Creative Commons Attribution (CC BY) license (<https://creativecommons.org/licenses/by/4.0/>).

## 1. Introduction

The formation of an ultrafine-grained (UFG) structure is favorable for the mechanical and processing properties of aluminum-based alloys. Typically, combining significant plastic deformation with further recrystallization is the main method to form an UFG structure in metallic alloys [1–3]. Severe plastic deformation (SPD) [4–7] is the most effective for processing an UFG structure in aluminum and its alloys [4,5,8–13]. Grain fragmentation and continuous dynamic/post-dynamic recrystallization [1,14] occur during SPD and result in the formation of an UFG structure with a predominant fraction of high-angle grain boundaries [15,16]. The disadvantages of the SPD methods include high-energy consumption and size limitations. Multi-directional forging (MDF) is a promising and relatively simple SPD technique providing UFG structure [17–19]. MDF reduces the grain size to 0.5–1 μm [20,21], and the sub-grain size to 0.2 μm [22] and significantly improves the strength of aluminum alloys. A positive MDF effect on grain refinement [23–27] and strength [18,23,24] was demonstrated for aluminum and magnesium based alloys [9,18,24–28]. The drawback of MDF is the strain inhomogeneity at different points of the sample during deformation. This effect results in a bimodality of the grain structure, i.e., areas containing fine recrystallized grains in the center and coarse weakly deformed grains at the periphery of the samples [25,29–31]. An increase in the cumulative strain increases the grain structure homogeneity upon MDF but also increases the processing time and cost [9,18,32,33]. A heterogeneous structure with coarse

and fine particles can help to refine grains and improves microstructural homogeneity. Coarse particles with sizes of  $\sim 1 \mu\text{m}$  refine the grains due to particle-stimulated nucleation (PSN), whereas nanoscale particles  $< 100 \text{ nm}$  inhibit grain growth and increase grain size stability via Zener pinning mechanism [34–39].

The particle stimulated nucleation effect is deeply studied [40–44]. The PSN is observed in heterogeneous alloys containing coarse undeformed particles of the secondary phases [45–48]. During the plastic deformation processes the areas around the particles accumulate lattice misorientations. It was demonstrated that the deformation process in polycrystals containing particles with a size greater than  $0.1 \mu\text{m}$  results in a formation of locally rotated regions (deformation zones) [49]. Those deformation zones act as a preferred site for the formation of nuclei of new grains during recrystallization. As reported by Humphreys [50], the nucleus of new grains originates on a pre-existing subgrain but not necessarily on in the interface boundary. Nucleation is forced by a movement of the low angle grain boundaries. The formation of the nuclei comes at a moment when the misorientation angle in the deformation zone exceeds a critical value required to form a high angle grain boundary. Nucleation strictly depends on the strain and particle parameters as particle size, volume fraction, and interparticle space. According to ref. [51], the grain size predicted on basis of PSN effect of recrystallization follows the equation  $D \sim d/f^{1/3}$ , where  $d$  is particle size and  $f$  is particle volume fraction. Thus, the PSN effect allows to refine grains through increasing the particle volume fraction and decreasing the particle size. Meanwhile, the critical particle size for PSN depends on the strain [50]. Following multiple researches, the optimal particle size for grain refinement via PSN is in a range of  $0.5\text{--}2 \mu\text{m}$  for Al alloys [50]. The coarse particles, required for PSN, in Al-based alloys are precipitated due to heterogenization annealing [52] or alloying with eutectic-forming elements, including Mn [53], Cu [54], Ca [55], Ni [56,57], Fe [58,59], Ce [40,60], etc.

To provide for the formation of nanoscale precipitates (dispersoids), the aluminum is usually alloyed with transition metals (TM), including rare earth (RE) metals [61–65]. These elements predominately have extremely low solubility in aluminum. However, the supersaturated solid solution of aluminum with TM can be formed through a solidification with an increased cooling rate [66]. Subsequent heat treatment of the supersaturated solid solution initiates its decomposition accompanied by the precipitation of nanoscale intermetallic particles. These particles effectively pin grain boundaries and suppress grain growth due to Zener pinning effect. The most effective dispersoid forming elements in aluminum alloys are Sc and Zr that form the  $L_{12}$ -structured phases of  $\text{Al}_3\text{Sc}$  and  $\text{Al}_3\text{Zr}$ , respectively [67,68]. It was demonstrated that the complex addition of both Sc and Zr in aluminum alloys is more effective than each element separately [69,70]. These elements form the complex  $L_{12}$ -structured phase  $\text{Al}_3(\text{Sc,Zr})$  [37,38,71,72]. Such dispersoids exhibit core–shell structure with Sc enriched core and Zr enriched shell [66,73]. Low diffusive Zr atoms significantly improve the thermal stability of particles whereas high diffusive Sc accelerates the nucleation of dispersoids [74] and strongly reduces the annealing time required to form a high number density of precipitates. MDF produces a fine-grained structure with a mean grain size of  $1\text{--}2 \mu\text{m}$  in the central part of the sample for Al-based alloys with  $L_{12}$ -structured precipitates ( $\sim 10 \text{ nm}$ ) and  $\text{Al}_6\text{Mn}$  precipitates ( $\sim 50 \text{ nm}$ ) [9,18,22,75]. However, Al-Mg-Sc-Zr based alloys demonstrated far better grain size stability at elevated temperatures [21]. The effectiveness of fine  $L_{12}$  precipitates and Zener pinning mechanism was evidenced for various SPD techniques [76,77]. Coarse particles of eutectic origin phases improve grain structure homogeneity during superplastic deformation in different Al-based alloys [58,78,79]. Meanwhile, the effectiveness of coarse particles and related PSN mechanism during MDF requires further investigation. The PSN effect is involved in grain refinement and grain structure homogeneity improvement upon MDF of Al-Mg-Mn-based alloys due to soluble  $\text{Al}_3\text{Mg}_2$  phase particles sized  $\sim 0.9 \mu\text{m}$  precipitating at heterogenization annealing [58]. The PSN effect intensifies with an increase in the particle size to  $1\text{--}2 \mu\text{m}$  due to smaller strains required. Thus, insoluble precipitates of eutectic origin phases with transition elements are potentially effective, their fraction and size are

controlled by alloying element content, solidification rate, and heat treatment regimes. Moreover, phases with transition metals demonstrate a good size stability and a high hardness at hot deformation temperatures, thus, proving to be more effective for PSN than soluble phases. In this work, the influence of Al<sub>3</sub>Ni coarse particle fraction on the microstructure and mechanical properties of multidirectional-forged Al-Mg-Zr-Sc-based alloys with various Ni contents were studied.

## 2. Materials and Methods

The compositions of the studied alloys are shown in Table 1. The following pure metals and master alloys were used for alloy preparation: 99.7 wt.% Al, 99.95 wt.% Mg, Al—20wt.% Ni, Al—4.3 wt.% Zr, Al—2.5 wt.% Sc. The alloys were prepared in a Nabertherm S3 resistance furnace (Nabertherm GmbH, Lilienthal, Germany), using graphite fireclay crucibles and cast into a copper-based water-cooled mold with internal dimensions of 20 mm × 40 mm × 100 mm. The cooling rate during the solidification process was ~ 15 K/s. Before casting, the melt was held at 830 °C for 10 min. The temperature of the melt was controlled by a Type K chromel-alumel thermocouple. The ingots were heat treated in a Nabertherm N30/65A air-forced convection furnace (Nabertherm GmbH, Lilienthal, Germany) with a temperature maintenance accuracy of ±1 °C. The ingots were subjected to a two-step homogenization with the first step at 360 °C for 8 h and subsequent second step at 400 °C for 4 h. After annealing the samples were cooled down to room temperature under air atmosphere.

**Table 1.** Chemical composition of studied alloys (wt.%).

Alloy Designation	Mg	Ni	Zr	Sc	Fe	Si	Al
1Ni	4.70	1.1	0.21	0.10	0.13	0.14	Bal.
2Ni	4.67	2.1	0.20	0.09	0.14	0.15	Bal.
4Ni	4.65	4.3	0.19	0.10	0.13	0.15	Bal.

The multi-directional forging (MDF) was carried out in a hydraulic press machine (Nordberg N3650E, Changshu Tongrun Auto Accessory Co., Ltd., Changshu, China) with a maximum load of 50 tons. The forging process was carried out in several steps at an initial crosshead speed of 5 mm/min at 350 °C. The logarithmic strain values per one pass and for the full forging cycle were 0.8 and 2.4, respectively. During each pass the sample was deformed along 2 axes, the sample shape being maintained. The samples were rotated through 90° after each pass for providing multiaxial deformation. The scheme of the applied MDF process is presented in [18]. Graphite lubricant was used to minimize the friction between the sample and the die. The samples were subjected to 15 forging passes (5 cycles).

The microstructural studies were carried out under a Tescan-VEGA3 LMH scanning electron microscope with a LaB<sub>6</sub> filament (Tescan Brno s.r.o., Kohoutovice, Czech Republic) equipped with an energy dispersive spectroscopy (EDS) detector (Oxford Instruments plc, Abingdon, UK) and an electron backscattered diffraction (EBSD) HKL NordlysMax detector (Oxford Instruments plc, Abingdon, UK). The images were obtained at an accelerating voltage of 20 kV in backscattered electron (BSE) mode with a working distance of 10–15 mm. The grain structure of samples in the as-cast state and after multidirectional forging was studied using a Carl Zeiss Axiovert 200MMAT (Carl Zeiss, Oberkochen, Germany) light microscope with a function of polarized light. The samples for light and scanning electron microscopy were prepared by mechanical grinding and polishing using a Struers LaboPol (Struers APS, Ballerup, Denmark) polishing machine. The grain structure was studied under a light microscope in polarized light that required additional anodizing of samples in Barker's reagent. The mean grain size was calculated using a linear secant method counting at least 300 grain boundaries per one state. The error bars of the mean

grain size were calculated for standard experimental data deviation at a 95% confidence interval.

The EBSD maps were obtained with a step of 0.4  $\mu\text{m}$  and a scan area of 250  $\mu\text{m} \times 250 \mu\text{m}$ . The analysis of the obtained maps was carried out using Aztec (EBSD) software (v.2.0, Oxford Instruments plc, Abingdon, UK). It was considered that the high-angle grain boundaries (HAGBs) exhibited a misorientation angle higher than  $15^\circ$  and low-angle grain boundaries (LAGBs) exhibited a misorientation angle of  $2\text{--}15^\circ$ .

Nanoscale dispersoids and the subgrain structure were analyzed using transmission electron microscopy (TEM) under a JEOL JEM-2100 microscope (JEOL Ltd., Tokyo, Japan) at an accelerating voltage of 200 kV. The TEM samples with 3 mm diameter were mechanically grinded to a 0.25 mm thickness and further electro-polished to process a hole using a Struers TenuPol-5 (Struers APS, Ballerup, Denmark) and A2-type electrolyte (Struers-produced) at a 21 V voltage and a temperature of  $0 \pm 4^\circ\text{C}$ . The mean size of coarse eutectic origin particles and nanoscale dispersoids was calculated through measuring the maximum particle diameter. For each studied alloy, the number of measurements was in the range of 200 to 300. The error bars of the dispersoid size were estimated experimentally using a standard deviation and a confidence probability of 0.95.

The mechanical properties of the studied materials (yield strength, ultimate tensile strength, and elongation-to-failure) at room temperature were studied using a uniaxial tensile test. The test was carried out by a Zwick Z250 universal testing machine (Zwick Roell Group, Ulm, Germany). The crosshead velocity during the test was 4 mm/min. For the tensile test, the samples with a gauge part length of 18 mm, a wideness of 6 mm, and a thickness of 1 mm were used. Three samples were tested for each studied alloy. The samples were cut from the as-forged alloys using a Charmilles Robofil 190 wire-electro discharge machine (Agie Charmilles, Geneva, Switzerland)

### 3. Results

#### 3.1. Microstructure of Alloys before MDF

The microstructures of the as-cast and as-homogenized alloys studied are shown in Figure 1. The as-cast alloys exhibited a similar grain size of  $200 \pm 40 \mu\text{m}$ . Dendrites of the aluminum-based solid solution (Al) and the Ni-enriched phase ( $\text{Al}_3\text{Ni}$ ) having a bright contrast were observed in the SEM micrographs for the as-homogenized samples. An increase in the Ni content led to an increase in the  $\text{Al}_3\text{Ni}$  volume fraction. For the 1Ni, 2Ni, and 4Ni alloys, the volume fractions of  $\text{Al}_3\text{Ni}$  particles were  $2.3 \pm 0.2$ ,  $3.6 \pm 0.2$ , and  $7.9 \pm 0.3\%$ , respectively.

Low temperature annealing at  $360^\circ\text{C}$  reduced dendrite liquation, whereas the morphology of the eutectic phase changed only slightly. The subsequent high-temperature annealing stage at  $420^\circ\text{C}$  provided for partial fragmentation and spheroidization of the  $\text{Al}_3\text{Ni}$  phase. The particles exhibited a near-spherical morphology with a shape coefficient of 0.8 and a mean size of  $0.8 \pm 0.1 \mu\text{m}$ . The particle size varied in a range of 0.3–2.8  $\mu\text{m}$ .

The dispersoids with a mean size of  $11 \pm 1 \text{ nm}$  precipitated in the studied alloys after homogenization. The superlattice reflections of the dispersoids in SAEDs are typical of the  $\text{L}_{12}$ -structured  $\text{Al}_3(\text{Sc,Zr})$  phase. The ordered positions of the superlattice reflections and the overlapping of the zone axis for the Al and  $\text{L}_{12}$  phases confirm the coherency of the dispersoids with the matrix.

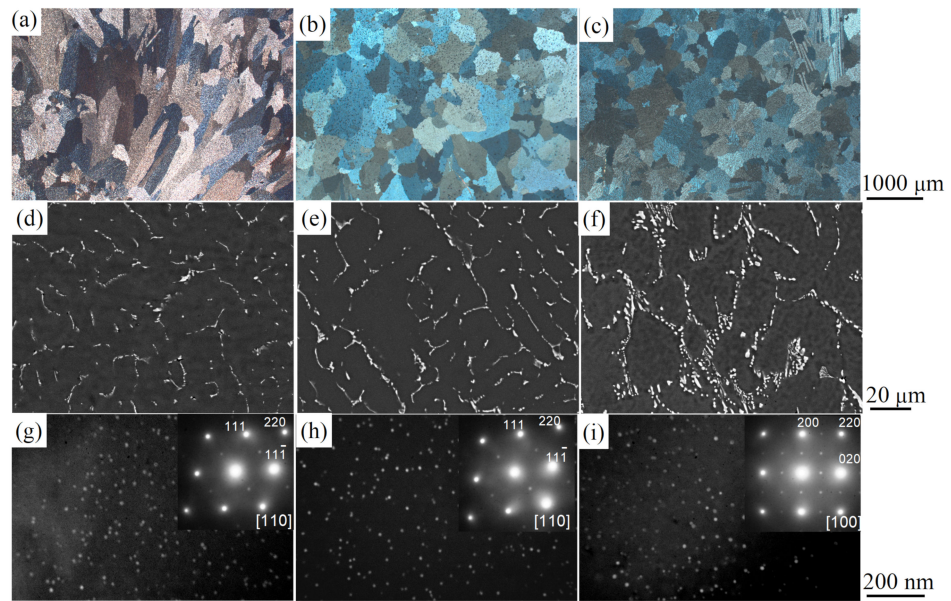


**Figure 1.** Images of the initial structure for (a,d,g) 1Ni, (b,e,h) 2Ni and (c,f,i) 4Ni alloys in (a–c) as-cast state and (d–i) as-homogenized state; (a–c) OM images (polarized light); (d–f) SEM-BSE images; (g–i) dark field TEM images and corresponding SAEDs (inserts). The images for different alloys are presented in the same magnification.

### 3.2. Stress–Strain Behavior during MDF

During multidirectional forging, the deformation occurred in two directions, being limited by the walls of the die in the third direction. The strain and stress values can be calculated as follows.

$$\varepsilon = \frac{2}{\sqrt{3}} \ln \left( \frac{h_0}{h_0 - \delta} \right) \quad (1)$$

$$\sigma = \frac{\sqrt{3} F (h_0 - \delta)}{2 V_0} \quad (2)$$

where  $h_0$  is the initial height of the sample,  $\delta$  is the stamp displacement,  $V_0$  is the sample volume, and  $F$  is the acting force.

The strain rate during forging with a constant stamp speed increased with time.

$$\dot{\varepsilon} = \frac{2}{\sqrt{3}} \frac{v}{h} \quad (3)$$

where  $v$  is the crosshead speed and  $h$  is the sample height.

During the compression of the samples with a size of 18 mm × 9 mm × 9 mm and a crosshead speed of 5 mm/min, the strain rate increased from  $5.2 \times 10^{-3}$  to  $1.1 \times 10^{-2} \text{ s}^{-1}$ . To consider the changes in the mean constant strain rate of  $\dot{\varepsilon}_{ref} = 0.0075 \text{ s}^{-1}$ , one should correct the stress values as follows:

$$\sigma_{ref} = \sigma(\dot{\varepsilon}) \left( \frac{\dot{\varepsilon}_{ref}}{\dot{\varepsilon}} \right)^m \quad (4)$$

where  $m$  is the strain rate sensitivity coefficient. For the studied type alloys and deformation regimes,  $m$  was taken as 0.2 [80].

Taking into account the increasing contact area between the sample and the die and considering the strain rate correction following Equation (4), the true stress vs. true strain curves exhibit a stable flow that typical of constant strain rate tests (Figure 2). Stable flow was observed in a strain range of 0.1–0.4 and was followed by an increase in the stress due to dynamic hardening or the contribution of friction between the die and sample. For

the 1Ni alloy, the flow stress decreased slightly with an increase in the cumulative strain (Figure 2d). With an increase in the Ni content to 4% and the fraction of the  $\text{Al}_3\text{Ni}$  phase to 8%, the stress decreased significantly during the first two cycles up to the cumulative strain  $\Sigma\varepsilon = 4-5$  (Figure 2d). The stress at higher cumulative strains differed but slightly.

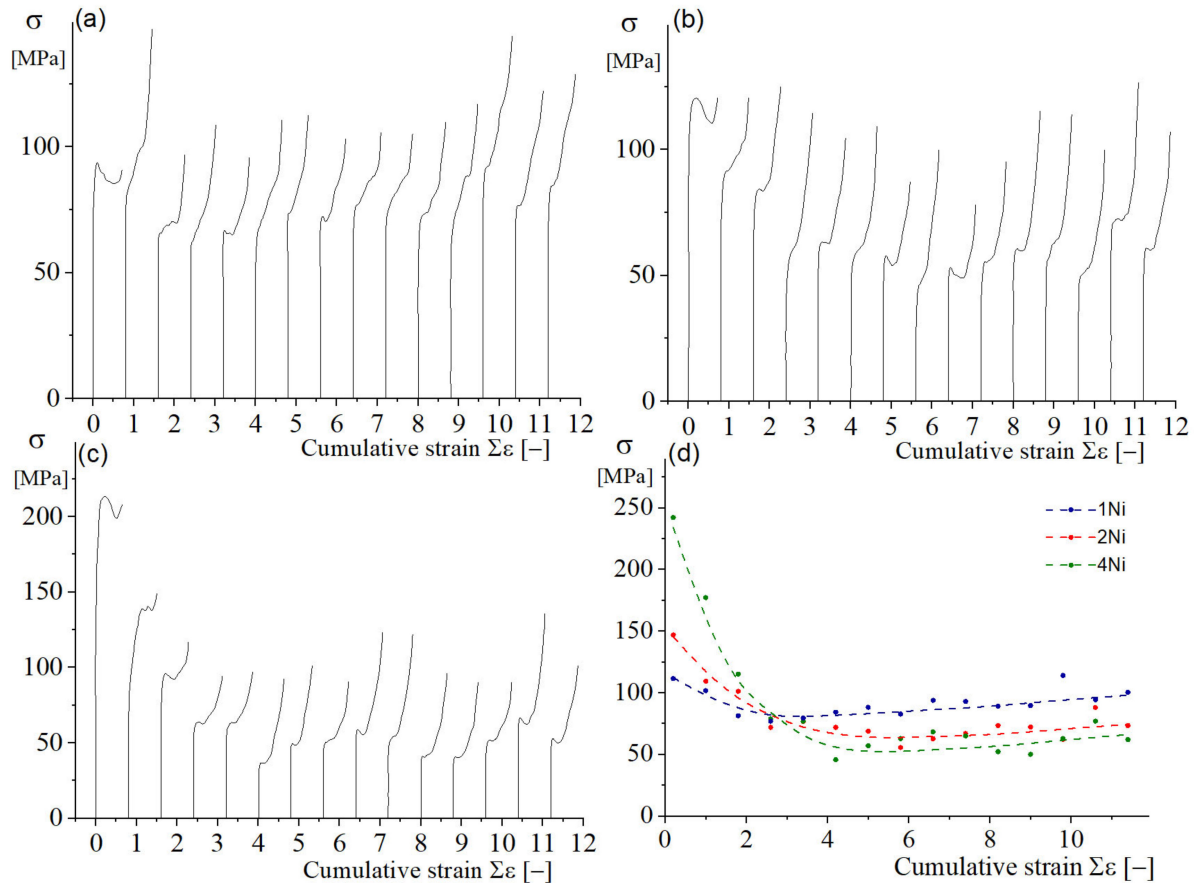


**Figure 2.** True stress vs. true strain curves for each full cycle of MDF for (a) 1Ni, (b) 2Ni, and (c) 4Ni alloys, and (d) true stress at 0.2 true strain as a function of cumulative strain.

The morphology of  $\text{Al}_3\text{Ni}$  particles changed with an increase in the number of cycles (Figure 3). The mean particle size and the aspect ratio did not change after processing with the cumulative strain  $\Sigma\varepsilon = 12$ . An increase in the number of cycles and in the Ni content provided for a uniform particle distribution.

By way of comparison between the grain structure and its homogeneity after MDF, low magnification images after 3 and 15 passes are presented in Figure 4. The microstructure of the alloys after the first MDF cycle was predominantly non-recrystallized with deformation bands in the grain interior (Figure 4a–c). A small fraction of equiaxed recrystallized grains was observed in the center of the 4Ni alloy sample. It is worth nothing that the recovery was predominant at a low strain. The grain structure after five cycles of forging was heterogeneous with areas of non-recrystallized deformed grains and fine-grained areas with a mean grain size of  $\sim 1 \mu\text{m}$ . An increase in the  $\text{Al}_3\text{Ni}$  volume fraction from 2% to 8% resulted in an increase in the volume fraction of fine recrystallized grains from 50% to 95%. Thus, the 4Ni alloy containing 8%  $\text{Al}_3\text{Ni}$  exhibited a near-completely recrystallized and highly uniform structure. Coarse non-recrystallized grains were predominately observed in the lower deformed periphery zones of the sample.

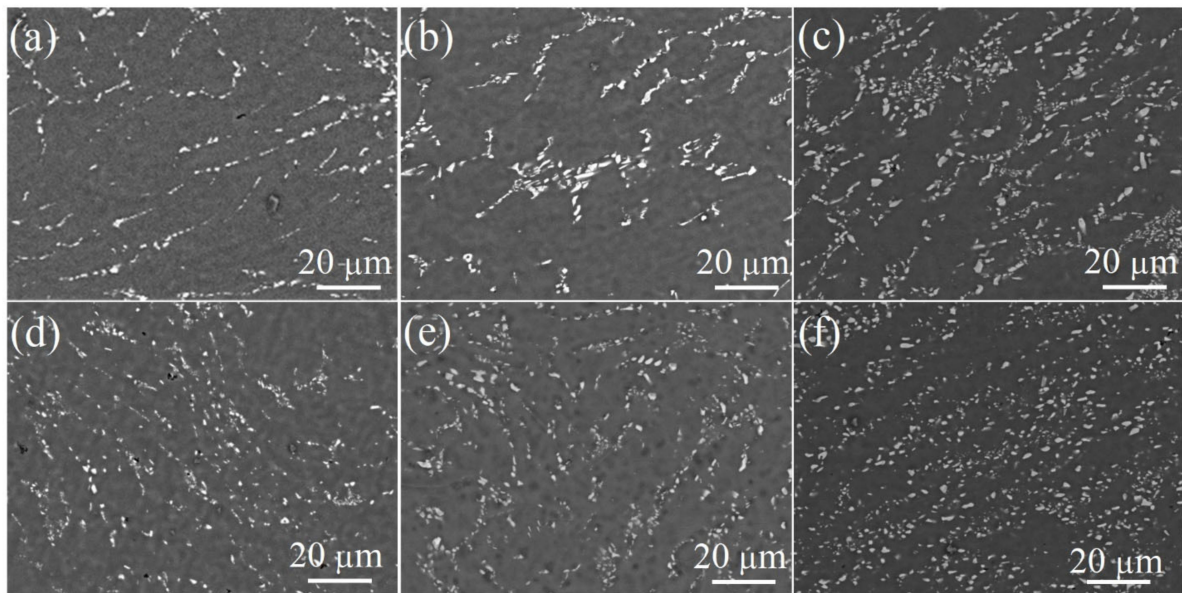


**Figure 3.** SEM-BSE images of (a,d) 1Ni, (b,e) 2Ni, and (c,f) 4Ni alloys after (a–c) 3 and (d–f) 15 MDF passes.

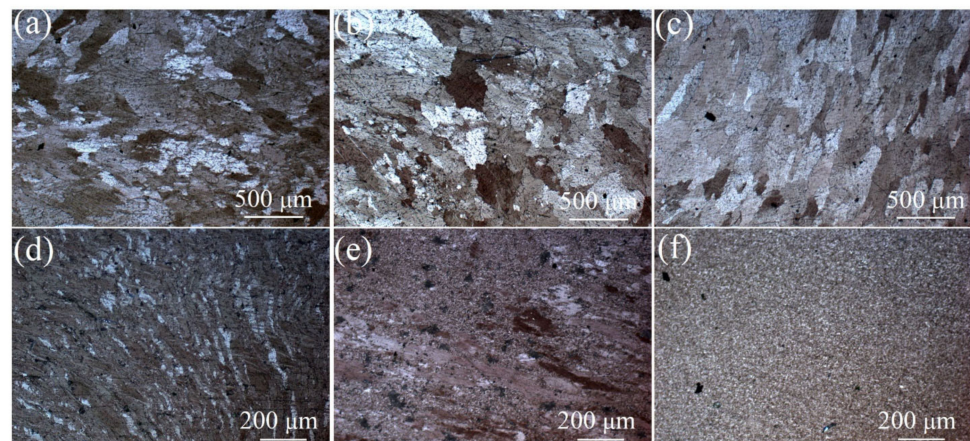


**Figure 4.** Grain structure of the (a,d) 1Ni, (b,e) 2Ni, and (c,f) 4Ni alloys (a–c) after 3 passes and (d–f) after 15 forging passes.

MDF treated samples with various Ni contents were analyzed by the EBSD technique after one and five MDF cycles (Figure 5). After the first three-pass cycle the structure was predominately non-recrystallized in all samples (Figure 5a–c). Fine recrystallized grains were observed at the grain boundaries of the deformed grains. The fraction of low angle grain boundaries was predominant. A bimodal grain structure produced after five cycles, featuring areas containing recrystallized grains surrounded by high-angle grain boundaries and areas containing non-recrystallized grains with a high subgrain fraction, was observed in the 2.3 and 3.6%  $\text{Al}_3\text{Ni}$  samples (Figure 5d,e). The 4% Ni sample (7.9%  $\text{Al}_3\text{Ni}$  phase) exhibited a completely recrystallized grain structure (Figure 5f). An increase in the Ni content improved the microstructural homogeneity and resulted in a decrease in the fraction of non-recrystallized grains and low-angle grain boundaries (Figures 5 and 6). The mean grain and subgrain sizes decreased with an increase in the  $\text{Al}_3\text{Ni}$  phase fraction.

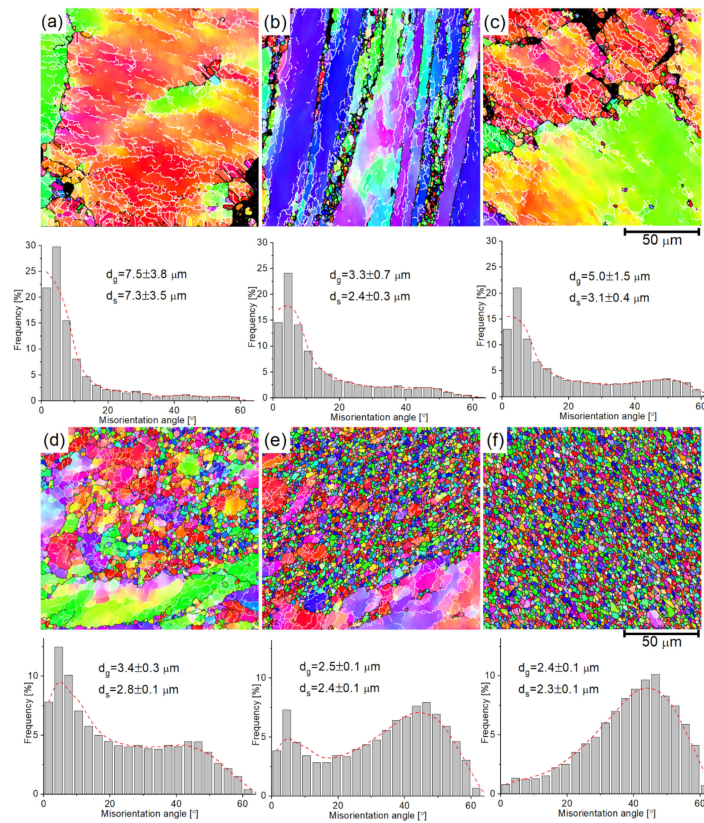


**Figure 5.** EBSD-IPF maps and grain boundary misorientation angle histograms for (a,d) 1Ni, (b,e) 2Ni, and (c,f) 4Ni alloys after (a–c) 3 and (d–f) 15 MDF passes.

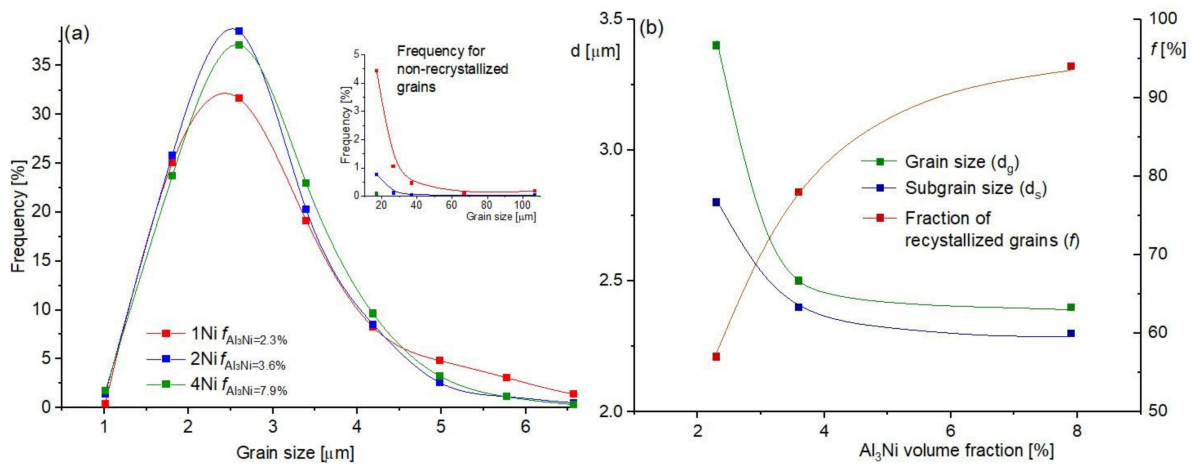


**Figure 6.** (a) Grain size distribution histogram; (b) dependencies of grain/subgrain size and fraction of recrystallized grains on the  $Al_3Ni$  volume fraction for studied alloys after 15 MDF passes.

The Kernel Average Misorientation (KAM) maps were calculated from the EBSD data for samples subjected to 15 MDF passes (Figure 7). The maps revealed increasing homogeneity of local misorientation with increase in  $Al_3Ni$  volume fraction. The mean values of local misorientation decreased with increasing Ni and were  $0.48^\circ$ ,  $0.43^\circ$ , and  $0.39^\circ$  for the 1Ni, 2Ni, and 4Ni alloys, respectively.



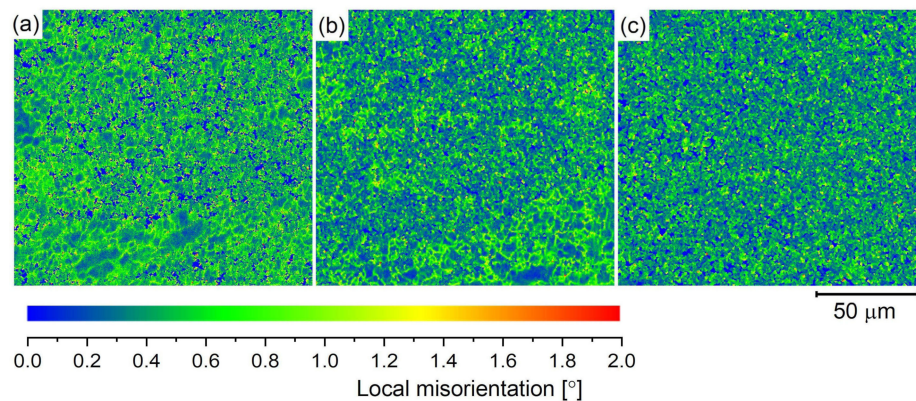


**Figure 7.** KAM maps for (a), 1Ni, (b) 2Ni, and (c) 4Ni alloys after 15 MDF passes.

The experimental data confirms that the hard and coarse eutectic particles stimulate the nucleation of new recrystallized grains during dynamic/post-dynamic recrystallization and significantly contribute to the formation of an ultrafine-grained structure after MDF. This effect intensified with an increase in the volume fraction of the particles.

TEM studies revealed a high dislocation density near coarse  $\text{Al}_3\text{Ni}$  particles, an increased dislocation density in the grain interior, dislocation walls and low angle grain boundaries. High angle grain boundaries dominated in the 4Ni alloy, but low angle grain boundaries were also observed (Figure 8).

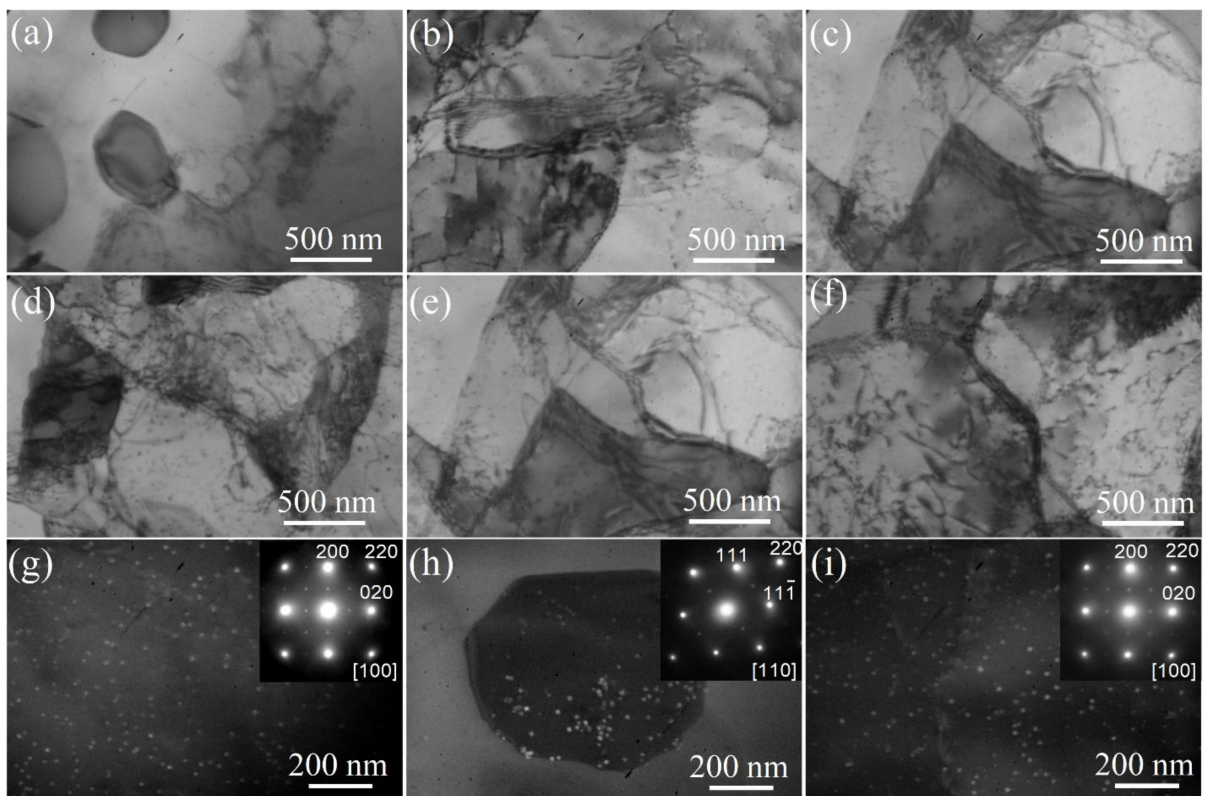


**Figure 8.** TEM images of (a,d,g) 1Ni, (b,e,h) 2Ni, and (c,f,i) 4Ni alloys after (a–c) 3 and (d–f) 15 MDF passes; (a–f)—bright field; (g–i)—dark field; inserts in (g–i)—SAEDs.

The morphology and size of  $L1_2$ -structured dispersoids did not change after five cycles of forging (Figure 8g–i). Ashby–Brown contrast (Figure 8f) and the ordered superlattice reflections in the SAEDs (inserts in Figure 8g–i) confirmed the coherence of the dispersoids with the aluminum matrix.

Mechanical properties at room temperature were analyzed after for MDF treated samples (Table 2). The stress vs. strain curves for the studied alloys are shown in Figure 9. Similar values of YS and UTS were observed for the 2 and 4% Ni alloys. The strength characteristics of the 1Ni alloy were lower. The values of elongation at fracture (El.) were  $12 \pm 3\%$  and  $14 \pm 4\%$  for the 1Ni and 2Ni alloys, respectively. An increase in the Ni content led to a decrease in the elongation to  $8 \pm 2\%$ .

**Table 2.** Room temperature mechanical properties of studied alloys after MDF.

Alloy	YS (MPa)	YTS (MPa)	El. (%)
1Ni	$290 \pm 5$	$343 \pm 5$	$12 \pm 3$
2Ni	$323 \pm 6$	$360 \pm 6$	$14 \pm 4$
4Ni	$323 \pm 6$	$353 \pm 5$	$8 \pm 2$

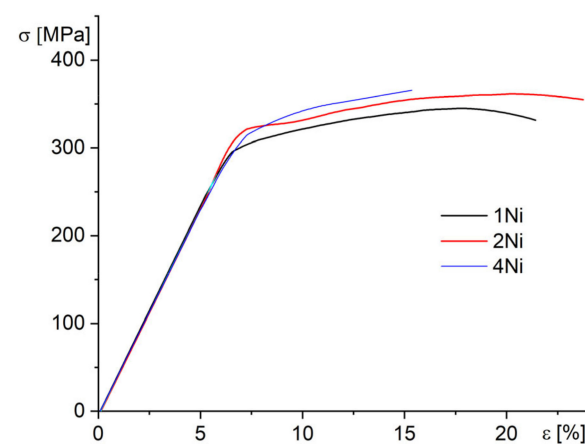


**Figure 9.** The stress vs. strain curves at room temperature for the studied alloys after 15 MDF passes.

#### 4. Discussion

The first homogenization step at  $350\text{ }^{\circ}\text{C}$  did not cause any significant microstructural changes and was aimed at intensifying the  $L_{12}$ -phase nucleation as was repeatedly demonstrated for Al-Mg-, Al-Zn-Mg-, and Al-Mg-Si-based alloys [81–83]. The second homogenization annealing step provided for a noticeable fragmentation of the  $\text{Al}_3\text{Ni}$  phase. The fragmentation and spheroidization of the eutectic particles during the heat treatment provided for a uniform particle distribution after thermomechanical treatment that agreed with [84]. The second homogenization step may also accelerate the precipitation kinetics [83,85] of the  $L_{12}$  phase. There were no differences observed in the precipitate's parameters for various alloys. This agreed with the atom probe tomography results presented in ref. [86,87], demonstrating that Ni was not observed in the precipitates since Ni cannot form a supersaturated solid solution in Al during solidification.

MDF facilitated the fragmentation of the  $\text{Al}_3\text{Ni}$  phase. The distribution homogeneity of the  $\text{Al}_3\text{Ni}$  particles increased with an increase in the  $\text{Al}_3\text{Ni}$  phase volume fraction, and hence, a more homogeneous distribution was observed for the 4Ni alloy. An increase in the number of MDF passes intensified fragmentation of particles and increased the particle distribution homogeneity. The  $L_{12}$ -phase did not change after MDF and exhibited an Ashby–Brown contrast and ordered superlattice reflections in the SAEDs. Fine precipitates of the  $L_{12}$ -phase contributed significantly to the thermal stability of the grain structure inhibiting the grain growth [70,85].

Dynamic recrystallization may occur through both discontinuous mechanisms involving grain nucleation near grain boundaries and coarse particles (PSN effect [50]) and continuous mechanism via an increase in the misorientation of the subgrain boundaries due to the accumulated strain. The PSN effect of hard particles of eutectic origin was confirmed for static recrystallization of cold-rolled alloys [40], dynamic recrystallization during

hot rolling [88] and compression [89], and superplastic deformation [78,88]. As shown for the studied alloys, the PSN of eutectic particles also played a significant role in the grain refinement during MDF, at large cumulative strains. Post-dynamic recrystallization processes can occur after the forging operation. In fact, the volume fraction of the particles noticeably affected the grain structure evolution. An increase in the volume fraction of the eutectic origin particles led to an increase in the structure homogeneity and a decrease in the mean grain size and fraction of the non-recrystallized grains. This confirms that  $\text{Al}_3\text{Ni}$  particles stimulate nucleation during recrystallization and contribute significantly to the formation of an ultrafine grained structure in the alloys studied.

An increase in the Ni content and the related  $\text{Al}_3\text{Ni}$  phase fraction also increased the strength characteristics of the alloys, but the high fraction of the particles reduced the elongation at fracture from 12–14% for the alloys with 2–3 %Ni to 8% for the alloy with 4 %Ni.

It was demonstrated that a bimodal particles size distribution provided for the formation of a homogeneous and thermally stable fine-grained structure after multidirectional forging and improved the strength characteristics. Coarse particles of the  $\text{Al}_3\text{Ni}$  phase led to PSN effect and nanoscale  $\text{L}_{12}$ -structured  $\text{Al}_3(\text{Sc,Zr})$  dispersoids inhibited grain boundaries migration due to a strong Zener pinning effect.

## 5. Conclusions

The microstructure evolution and deformation behavior of the  $\text{Al-5.7Mg-}x\text{Ni-0.2Zr-0.1Sc}$  ( $x = 1, 2$  and 4%) alloys during multidirectional forging at 350 °C and cumulative strains of 2.4–12 were studied. The main conclusions are drawn as follows.

The  $\text{L}_{12}$  precipitates of the  $\text{Al}_3(\text{Sc,Zr})$  phase had a size of  $11 \pm 1$  nm and maintained their morphology, size, and coherency with the Al matrix during high-temperature multidirectional forging. The  $\text{Al}_3\text{Ni}$  phase particles of eutectic origin were refined and spheroidized, and their mean size was  $0.8 \pm 0.1$   $\mu\text{m}$  and aspect ratio was 0.8 for the alloys studied. Due to the particle stimulated nucleation effect of the  $\text{Al}_3\text{Ni}$  phase, an increase in its volume fraction from 2.3 to 7.9% with an increase in the Ni content from 1 to 4% raised the volume fraction of fine recrystallized grains from 50% to 95%, significantly improved the microstructural homogeneity and reduced the grain size from  $3.4 \pm 0.1$  to  $2.4 \pm 0.1$   $\mu\text{m}$ .

The yield strength and ultimate tensile strength increased from 290 MPa and 340 MPa, respectively, for the alloy with 1% Ni to 320 MPa and 360 MPa, respectively, for the alloys with 2–4% Ni. Meanwhile, the elongation at fracture decreased from 12–14% for the alloys with 1–2%Ni to 8% for the 4% Ni alloy. Thus, the alloying of the Al-Mg-Sc-Zr alloy with 2% Ni and multidirectional forging treatment provided both high strength and good ductility.

**Author Contributions:** M.S.K.: Investigation; Methodology; Data curation. A.G.M.: Writing—Original draft; Investigation; Formal analysis; Project administration; Resources. M.C.: Investigation; Methodology; A.A.K.: Validation; Data curation. A.V.M.: Supervision; Conceptualization; Investigation; Software; Writing—review and editing. All authors have read and agreed to the published version of the manuscript.

**Funding:** The structure evolution during MDF was studied in the framework of the Russian Science Foundation, Grant No. 22-79-00253. The structure analysis in the as-cast and as-homogenized states was performed in the framework of the state task to MISIS University project code of FSME-2023-0005.

**Institutional Review Board Statement:** Not applicable.

**Informed Consent Statement:** Not applicable.

**Data Availability Statement:** The raw/processed data required to reproduce these findings cannot be shared at this time as the data also forms part of an ongoing study.

**Acknowledgments:** Authors are acknowledged to members of Scientific School HIII-1752.2022.4 for a helpful discussion of the studied phenomena.

**Conflicts of Interest:** The authors declare no conflict of interest.

## References

1. Sakai, T.; Belyakov, A.; Kaibyshev, R.; Miura, H.; Jonas, J.J. Dynamic and Post-Dynamic Recrystallization under Hot, Cold and Severe Plastic Deformation Conditions. *Prog. Mater. Sci.* **2014**, *60*, 130–207. [[CrossRef](#)]
2. Kawasaki, M.; Ahn, B.; Kumar, P.; Jang, J.I.; Langdon, T.G. Nano- and Micro-Mechanical Properties of Ultrafine Grained Materials Processed by Severe Plastic Deformation. *Adv. Eng. Mater.* **2017**, *19*, 1600578. [[CrossRef](#)]
3. Murashkin, M.; Medvedev, A.; Kazykhanov, V.; Krokhin, A.; Raab, G.; Enikeev, N.; Valiev, R.Z. Enhanced Mechanical Properties and Electrical Conductivity in Ultrafine-Grained Al 6101 Alloy Processed via ECAP-Conform. *Metals* **2015**, *5*, 2148–2164. [[CrossRef](#)]
4. Langdon, T.G. Twenty-Five Years of Ultrafine-Grained Materials: Achieving Exceptional Properties through Grain Refinement. *Acta Mater.* **2013**, *61*, 7035–7059. [[CrossRef](#)]
5. Valiev, R.Z.; Zhilyaev, A.P.; Langdon, T.G. *Bulk Nanostructured Materials: Fundamentals and Applications*; John Wiley & Sons Inc.: New York, NY, USA, 2014.
6. Avtokratova, E.; Sitdikov, O.; Mukhametdinova, O.; Markushev, M.; Murty, S.N.; Prasad, M.J.N.V.; Kashyap, B.P. Microstructural Evolution in Al–Mg–Sc–Zr Alloy during Severe Plastic Deformation and Annealing. *J. Alloys Compd.* **2016**, *673*, 182–194. [[CrossRef](#)]
7. Zayed, E.M.; Shazly, M.; El-Sabbagh, A.; El-Mahallawy, N.A. Deformation Behavior and Properties of Severe Plastic Deformation Techniques for Bulk Materials: A Review. *Heliyon* **2023**, *9*, e16700. [[CrossRef](#)] [[PubMed](#)]
8. Asadi, S.; Kazeminezhad, M. Multi Directional Forging of 2024 Al Alloy After Different Heat Treatments: Microstructural and Mechanical Behavior. *Trans. Indian Inst. Met.* **2017**, *70*, 1707–1719. [[CrossRef](#)]
9. Kishchik, M.S.; Mikhaylovskaya, A.V.; Kotov, A.D.; Mosleh, A.O.; AbuShanab, W.S.; Portnoy, V.K. Effect of Multidirectional Forging on the Grain Structure and Mechanical Properties of the Al–Mg–Mn Alloy. *Materials* **2018**, *11*, 2166. [[CrossRef](#)] [[PubMed](#)]
10. Markushev, M.V.; Avtokratova, E.V.; Sitdikov, O.S. Effect of the Initial State on Nanostructuring and Strengthening of Middle- and High-Strength Age-Hardenable Aluminum Alloys under Severe Plastic Deformation (Review). *Lett. Mater.* **2017**, *7*, 459–464. [[CrossRef](#)]
11. Buranova, Y.; Kulitskiy, V.; Peterlechner, M.; Mogucheva, A.; Kaibyshev, R.; Divinski, S.V.; Wilde, G. Al<sub>3</sub>(Sc,Zr)-Based Precipitates in Al–Mg Alloy: Effect of Severe Deformation. *Acta Mater.* **2017**, *124*, 210–224. [[CrossRef](#)]
12. Sabirov, I.; Murashkin, M.Y.; Valiev, R.Z. Nanostructured Aluminium Alloys Produced by Severe Plastic Deformation: New Horizons in Development. *Mater. Sci. Eng. A* **2013**, *560*, 1–24. [[CrossRef](#)]
13. Valiev, R.Z.; Sabirov, I.; Zhilyaev, A.P.; Langdon, T.G. Bulk Nanostructured Metals for Innovative Applications. *JOM* **2012**, *64*, 1134–1142. [[CrossRef](#)]
14. Cao, Y.; Ni, S.; Liao, X.; Song, M.; Zhu, Y. Structural Evolutions of Metallic Materials Processed by Severe Plastic Deformation. *Mater. Sci. Eng. R Rep.* **2018**, *133*, 1–59. [[CrossRef](#)]
15. Sakai, T.; Miura, H.; Goloborodko, A.; Sitdikov, O. Continuous Dynamic Recrystallization during the Transient Severe Deformation of Aluminum Alloy 7475. *Acta Mater.* **2009**, *57*, 153–162. [[CrossRef](#)]
16. Sitdikov, O.; Sakai, T.; Goloborodko, A.; Miura, H.; Kaibyshev, R. Effect of Pass Strain on Grain Refinement in 7475 Al Alloy during Hot Multidirectional Forging. *Mater. Trans.* **2004**, *45*, 2232–2238. [[CrossRef](#)]
17. Mulyukov, R.R.; Imayev, R.M.; Nazarov, A.A. Production, Properties and Application Prospects of Bulk Nanostructured Materials. *J. Mater. Sci.* **2008**, *43*, 7257–7263. [[CrossRef](#)]
18. Mikhaylovskaya, A.V.; Kotov, A.D.; Kishchik, M.S.; Prosviryakov, A.S.; Portnoy, V.K. The Effect of Isothermal Multi-Directional Forging on the Grain Structure, Superplasticity, and Mechanical Properties of the Conventional Al–Mg-Based Alloy. *Metals* **2019**, *9*, 33. [[CrossRef](#)]
19. Aoba, T.; Kobayashi, M.; Miura, H. Effects of Aging on Mechanical Properties and Microstructure of Multi-Directionally Forged 7075 Aluminum Alloy. *Mater. Sci. Eng. A* **2017**, *700*, 220–225. [[CrossRef](#)]
20. Zhu, Q.; Li, L.; Ban, C.; Zhao, Z.; Zuo, Y.; Cui, J. Structure Uniformity and Limits of Grain Refinement of High Purity Aluminum during Multi-Directional Forging Process at Room Temperature. *Trans. Nonferrous Met. Soc. China* **2014**, *24*, 1301–1306. [[CrossRef](#)]
21. Padap, A.K.; Chaudhari, G.P.; Nath, S.K.; Pancholi, V. Ultrafine-Grained Steel Fabricated Using Warm Multiaxial Forging: Microstructure and Mechanical Properties. *Mater. Sci. Eng. A* **2009**, *527*, 110–117. [[CrossRef](#)]
22. Sitdikov, O.; Garipova, R.; Avtokratova, E.; Mukhametdinova, O.; Markushev, M. Effect of Temperature of Isothermal Multidirectional Forging on Microstructure Development in the Al–Mg Alloy with Nano-Size Aluminides of Sc and Zr. *J. Alloys Compd.* **2018**, *746*, 520–531. [[CrossRef](#)]
23. Miura, H.; Nakamura, W. Microstructure and Mechanical Properties of Mg–8Al Alloy Fabricated by Room-Temperature Multi-Directional Forging. *Philos. Mag. Lett.* **2013**, *93*, 601–607. [[CrossRef](#)]
24. Li, J.; Liu, J.; Cui, Z. Microstructures and Mechanical Properties of AZ61 Magnesium Alloy after Isothermal Multidirectional Forging with Increasing Strain Rate. *Mater. Sci. Eng. A* **2015**, *643*, 32–36. [[CrossRef](#)]
25. Armstrong, P.E.; Hockett, J.E.; Sherby, O.D. Large Strain Multidirectional Deformation of 1100 Aluminum at 300 K. *J. Mech. Phys. Solids* **1982**, *30*, 37–58. [[CrossRef](#)]
26. Rao, P.N.; Singh, D.; Jayaganthan, R. Mechanical Properties and Microstructural Evolution of Al 6061 Alloy Processed by Multidirectional Forging at Liquid Nitrogen Temperature. *Mater. Des.* **2014**, *56*, 97–104. [[CrossRef](#)]

27. Estrin, Y.; Vinogradov, A. Extreme Grain Refinement by Severe Plastic Deformation: A Wealth of Challenging Science. *Acta Mater.* **2013**, *61*, 782–817. [[CrossRef](#)]
28. Mirzadeh, H. Grain Refinement of Magnesium Alloys by Dynamic Recrystallization (DRX): A Review. *J. Mater. Res. Technol.* **2023**, *25*, 7050–7077. [[CrossRef](#)]
29. Buckingham, R.C.; Argyrakis, C.; Hardy, M.C.; Biroscas, S. The Effect of Strain Distribution on Microstructural Developments during Forging in a Newly Developed Nickel Base Superalloy. *Mater. Sci. Eng. A* **2016**, *654*, 317–328. [[CrossRef](#)]
30. Xu, X.; Zhang, Q.; Hu, N.; Huang, Y.; Langdon, T.G. Using an Al-Cu Binary Alloy to Compare Processing by Multi-Axial Compression and High-Pressure Torsion. *Mater. Sci. Eng. A* **2013**, *588*, 280–287. [[CrossRef](#)]
31. Jandaghi, M.R.; Pouraliakbar, H.; Shiran, M.K.G.; Khalaj, G.; Shirazi, M. On the Effect of Non-Isothermal Annealing and Multi-Directional Forging on the Microstructural Evolutions and Correlated Mechanical and Electrical Characteristics of Hot-Deformed Al-Mg Alloy. *Mater. Sci. Eng. A* **2016**, *657*, 431–440. [[CrossRef](#)]
32. Miura, H.; Nakao, Y.; Sakai, T. Enhanced Grain Refinement by Mechanical Twinning in a Bulk Cu-30mass%Zn during Multi-Directional Forging. *Mater. Trans.* **2007**, *48*, 2539–2541. [[CrossRef](#)]
33. Ringeval, S.; Piot, D.; Desrayaud, C.; Driver, J.H. Texture and Microtexture Development in an Al-3Mg-Sc(Zr) Alloy Deformed by Triaxial Forging. *Acta Mater.* **2006**, *54*, 3095–3105. [[CrossRef](#)]
34. Zolotarevskiy, V.S.; Dobrojinskaja, R.I.; Cheverikin, V.V.; Khamnagdaeva, E.A.; Pozdniakov, A.V.; Levchenko, V.S.; Besogonova, E.S. Evolution of the Structure and Mechanical Properties of Sheets of the Al-4.7 Mg-0.32 Mn-0.21 Sc-0.09 Zr Alloy Due to Deformation Accumulated upon Rolling. *Phys. Met. Metallogr.* **2016**, *117*, 1163–1169. [[CrossRef](#)]
35. Zolotarevskiy, V.S.; Dobrozinskaya, R.I.; Cheverikin, V.V.; Khamnagdaeva, E.A.; Pozdniakov, A.V.; Levchenko, V.S.; Besogonova, E.S. Strength and Substructure of Al-4.7Mg-0.32Mn-0.21Sc-0.09Zr Alloy Sheets. *Phys. Met. Metallogr.* **2017**, *118*, 407–414. [[CrossRef](#)]
36. Mikhaylovskaya, A.V.; Portnoy, V.K.; Mochugovskiy, A.G.; Zadorozhnyy, M.Y.; Tabachkova, N.Y.; Golovin, I.S. Effect of Homogenisation Treatment on Precipitation, Recrystallisation and Properties of Al-3% Mg-TM Alloys (TM = Mn, Cr, Zr). *Mater. Des.* **2016**, *109*, 197–208. [[CrossRef](#)]
37. Ning, J.L.; Jiang, D.M. Influence of Zr Addition on the Microstructure Evolution and Thermal Stability of Al-Mg-Mn Alloy Processed by ECAP at Elevated Temperature. *Mater. Sci. Eng. A* **2007**, *452*, 552–557. [[CrossRef](#)]
38. Jones, M.J.; Humphreys, F.J. Interaction of Recrystallization and Precipitation: The Effect of Al<sub>3</sub>Sc on the Recrystallization Behaviour of Deformed Aluminium. *Acta Mater.* **2003**, *51*, 2149–2159. [[CrossRef](#)]
39. Robson, J.D. A New Model for Prediction of Dispersoid Precipitation in Aluminium Alloys Containing Zirconium and Scandium. *Acta Mater.* **2004**, *52*, 1409–1421. [[CrossRef](#)]
40. Mikhaylovskaya, A.V.; Ryazantseva, M.A.; Portnoy, V.K. Effect of Eutectic Particles on the Grain Size Control and the Superplasticity of Aluminium Alloys. *Mater. Sci. Eng. A* **2011**, *528*, 7306–7309. [[CrossRef](#)]
41. Humphreys, F.J. The Nucleation of Recrystallization at Second Phase Particles in Deformed Aluminium. *Acta Metall.* **1977**, *25*, 1323–1344. [[CrossRef](#)]
42. Song, X.; Rettenmayr, M. Modeling Recrystallization in a Material Containing Fine and Coarse Particles. *Comput. Mater. Sci.* **2007**, *40*, 234–245. [[CrossRef](#)]
43. Nieh, T.G.; Wadsworth, J.; Sherby, O.D. *Superplasticity in Metals and Ceramics*; Cambridge University Press: Cambridge, UK, 1997; ISBN 9780521561051.
44. Khani, S.; Kazeminezhad, M.; Logé, R.; Khani Moghanaki, S.; Kazeminezhad, M.; Logé, R. Recrystallization Behavior of Multi-Directionally Forged over-Aged and Solution Treated Al-Cu-Mg Alloy during Non-Isothermal Annealing. *Mater. Des.* **2017**, *132*, 250–256. [[CrossRef](#)]
45. Wang, X.-Y.; Jiang, J.-T.; Li, G.-A.; Wang, X.-M.; Shao, W.-Z.; Zhen, L. Particle-Stimulated Nucleation and Recrystallization Texture Initiated by Coarsened Al<sub>2</sub>CuLi Phase in Al-Cu-Li Alloy. *J. Mater. Res. Technol.* **2021**, *10*, 643–650. [[CrossRef](#)]
46. Lei, X.; Zhang, Y.; Sun, J.; Bachmann, F.; Yang, X.; Sanders, R.E.; Juul Jensen, D. Particle Stimulated Nucleation Revisited in Three Dimensions: A Laboratory-Based Multimodal X-Ray Tomography Investigation. *Mater. Res. Lett.* **2021**, *9*, 65–70. [[CrossRef](#)]
47. Jeon, J.; Lee, S.; Kyeong, J.; Shin, S.; Kang, H. Effect of Geometrical Parameters of Microscale Particles on Particle-Stimulated Nucleation and Recrystallization Texture of Al-Si-Mg-Cu-Based Alloy Sheets. *Materials* **2022**, *15*, 7924. [[CrossRef](#)]
48. Zang, Q.; Chen, H.; Lee, Y.-S.; Yu, H.; Kim, M.-S.; Kim, H.-W. Improvement of Anisotropic Tensile Properties of Al-7.9Zn-2.7Mg-2.0Cu Alloy Sheets by Particle Stimulated Nucleation. *J. Alloys Compd.* **2020**, *828*, 154330. [[CrossRef](#)]
49. Humphreys, F.J.; Kalu, P.N. The Plasticity of Particle-Containing Polycrystals. *Acta Metall. Mater.* **1990**, *38*, 917–930. [[CrossRef](#)]
50. Humphreys, F.J.; Hatherly, M. *Recrystallization and Related Annealing Phenomena*, 2nd ed.; Pergamon Press: Oxford, UK, 1995.
51. Humphreys, F.J.; Miller, W.S.; Djazeb, M.R. Microstructural Development during Thermomechanical Processing of Particulate Metal-Matrix Composites. *Mater. Sci. Technol.* **1990**, *6*, 1157–1166. [[CrossRef](#)]
52. Wert, J.A.; Paton, N.E.; Hamilton, C.H.; Mahoney, M.W. Grain Refinement in 7075 Aluminum by Thermomechanical Processing. *Metall. Trans. A* **1981**, *12*, 1267–1276. [[CrossRef](#)]
53. Kudo, T.; Goto, A.; Saito, K. High Strain Rate Blow Formability of Newly Developed Al-Mg-High-Mn Alloy. *Mater. Sci. Forum* **2012**, *735*, 271–277. [[CrossRef](#)]
54. Pozdniakov, A.V.; Barkov, R.Y.; Amer, S.M.; Levchenko, V.S.; Kotov, A.D.; Mikhaylovskaya, A.V. Microstructure, Mechanical Properties and Superplasticity of the Al-Cu-Y-Zr Alloy. *Mater. Sci. Eng. A* **2019**, *758*, 28–35. [[CrossRef](#)]

55. Moore, D.M.; Morris, L.R. A New Superplastic Aluminum Sheet Alloy. *Mater. Sci. Eng.* **1980**, *43*, 85–92. [[CrossRef](#)]
56. Churyumov, A.Y.; Mikhaylovskaya, A.V.; Bazlov, A.I.; Tsarkov, A.A.; Kotov, A.D.; Aksenov, S.A. Influence of Al<sub>3</sub>Ni Crystallisation Origin Particles on Hot Deformation Behaviour of Aluminium Based Alloys. *Philos. Mag.* **2017**, *97*, 572–590. [[CrossRef](#)]
57. Taylor, S.; Janik, V.; Grimes, R.; Dashwood, R. Study on the Influence of Nickel Additions on AA7020 Formability Under Superplastic Forming Like Conditions. *Met. Mater. Int.* **2023**, *29*, 2597–2604. [[CrossRef](#)]
58. Kishchik, A.A.; Mikhaylovskaya, A.V.; Kotov, A.D.; Rofman, O.V.; Portnoy, V.K. Al-Mg-Fe-Ni Based Alloy for High Strain Rate Superplastic Forming. *Mater. Sci. Eng. A* **2018**, *718*, 190–197. [[CrossRef](#)]
59. Mikhaylovskaya, A.V.; Kishchik, A.A.; Kotov, A.D.; Rofman, O.V.; Tabachkova, N.Y. Precipitation Behavior and High Strain Rate Superplasticity in a Novel Fine-Grained Aluminum Based Alloy. *Mater. Sci. Eng. A* **2019**, *760*, 37–46. [[CrossRef](#)]
60. Mikhaylovskaya, A.V.; Kishchik, A.A.; Tabachkova, N.Y.; Kotov, A.D.; Cheverikin, V.V.; Bazlov, A.I. Microstructural Characterization and Tensile Properties of Al-Mg-Fe-Ce Alloy at Room and Elevated Temperatures. *JOM* **2020**, *72*, 1619–1626. [[CrossRef](#)]
61. Zupanič, F.; Žist, S.; Albu, M.; Letofsky-Papst, I.; Burja, J.; Vončina, M.; Bončina, T. Dispersoids in Al-Mg-Si Alloy AA 6086 Modified by Sc and Y. *Materials* **2023**, *16*, 2949. [[CrossRef](#)] [[PubMed](#)]
62. Amer, S.M.; Barkov, R.Y.; Prosviryakov, A.S.; Pozdniakov, A.V. Structure and Properties of New Wrought Al-Cu-Y- and Al-Cu-Er-Based Alloys. *Phys. Met. Metallogr.* **2021**, *122*, 915–922. [[CrossRef](#)]
63. Liu, F.; Zhu, X.; Qin, J.; Zhou, W.; Ling, J.; Dong, Q.; Yu, J.; Nagaumi, H.; Zhang, B. Effect of Mn/Cr Ratio on Precipitation Behaviors of  $\alpha$ -Al(FeMnCr)Si Dispersoids and Mechanical Properties of Al-Mg-Si-Cu Alloys. *Mater. Sci. Eng. A* **2022**, *860*, 144269. [[CrossRef](#)]
64. Li, Q.; Huang, G.; Cao, Y.; Zhang, C.; He, J.; Jiang, H.; Lin, L.; Liu, Q. Microstructure Refinement, Strengthening and Ductilization Mechanisms in Al-Mg-Mn-Er-Zr Alloy with High Mn Content by Friction Stir Processing. *Mater. Charact.* **2022**, *189*, 111939. [[CrossRef](#)]
65. Deng, Y.; Zhang, G.; Yang, Z.; Xu, G. Microstructure Characteristics and Mechanical Properties of New Aerospace Al-Mg-Mn Alloys with Al<sub>3</sub>(Sc<sub>1-x</sub>Zr<sub>x</sub>) or Al<sub>3</sub>(Er<sub>1-x</sub>Zr<sub>x</sub>) Nanoparticles. *Mater. Charact.* **2019**, *153*, 79–91. [[CrossRef](#)]
66. Monastyrskaya, T.O.; Berezina, A.L.; Molebny, O.A.; Kotko, A.V. Effect of Alloying with Transition Metals on the Aging of Anomalously Supersaturated Solid Solution of Al-Mg Alloys. *Appl. Nanosci.* **2022**, *12*, 513–521. [[CrossRef](#)]
67. Dorin, T.; Jiang, L.; Langan, T. Formation of Al<sub>3</sub>Sc Dispersoids and Associated Strengthening. In *TMS Annual Meeting & Exhibition*; Springer Nature: Cham, Switzerland, 2023; pp. 1207–1212.
68. Croteau, J.R.; Jung, J.-G.; Whalen, S.A.; Darsell, J.; Mello, A.; Holstine, D.; Lay, K.; Hansen, M.; Dunand, D.C.; Vo, N.Q. Ultrafine-Grained Al-Mg-Zr Alloy Processed by Shear-Assisted Extrusion with High Thermal Stability. *Scr. Mater.* **2020**, *186*, 326–330. [[CrossRef](#)]
69. Liu, Y.; Zhang, C.-C.; Zhang, X.-Y.; Huang, Y.-C. Understanding Grain Refinement of Sc Addition in a Zr Containing Al-Zn-Mg-Cu Aluminum Alloy from Experiments and First-Principles. *Intermetallics* **2020**, *123*, 106823. [[CrossRef](#)]
70. Mochugovskiy, A.G.; Mikhaylovskaya, A.V. Comparison of Precipitation Kinetics and Mechanical Properties in Zr and Sc-Bearing Aluminum-Based Alloys. *Mater. Lett.* **2020**, *275*, 128096. [[CrossRef](#)]
71. Robson, J.D.; Prangnell, P.B. Dispersoid Precipitation and Process Modelling in Zirconium Containing Commercial Aluminum Alloys. *Acta Mater.* **2001**, *49*, 599–613. [[CrossRef](#)]
72. Mochugovskiy, A.G.; Tabachkova, N.Y.; Ghayoumabadi, M.E.; Cheverikin, V.V.; Mikhaylovskaya, A.V. Joint Effect of Quasicrystalline Icosahedral and L12-Structured Phases Precipitation on the Grain Structure and Mechanical Properties of Aluminum-Based Alloys. *J. Mater. Sci. Technol.* **2021**, *87*, 196–206. [[CrossRef](#)]
73. Xue, C.; Wang, S.; Zhang, Y.; Tian, G.; Yang, X.; Chang, X.; Ke, Y.; Xie, Z.; Wang, J. Uncovering the Kinetics of Li-Rich Clusters and Monodisperse Core-Shell Al<sub>3</sub>(Zr, Sc) Structures in Al-Li-Cu Alloys. *Mater. Sci. Eng. A* **2023**, *881*, 145393. [[CrossRef](#)]
74. Wang, Y.; Zhang, S.; Wu, R.; Turakhodjaev, N.; Hou, L.; Zhang, J.; Betsofen, S. Coarsening Kinetics and Strengthening Mechanisms of Core-Shell Nanoscale Precipitates in Al-Li-Yb-Er-Sc-Zr Alloy. *J. Mater. Sci. Technol.* **2021**, *61*, 197–203. [[CrossRef](#)]
75. Sitdikov, O.; Avtokratova, E.; Markushev, M. Development of Ultrafine Grain Structure in an Al-Mg-Mn-Sc-Zr Alloy During High-Temperature Multidirectional Isothermal Forging. *Met. Mater. Int.* **2021**, *27*, 2743–2755. [[CrossRef](#)]
76. Kaibyshev, R.; Avtokratova, E.; Apollonov, A.; Davies, R. High Strain Rate Superplasticity in an Al-Mg-Sc-Zr Alloy Subjected to Simple Thermomechanical Processing. *Scr. Mater.* **2006**, *54*, 2119–2124. [[CrossRef](#)]
77. Sitdikov, O.; Avtokratova, E.; Markushev, M. Influence of Strain Rate on Grain Refinement in the Al-Mg-Sc-Zr Alloy during High-Temperature Multidirectional Isothermal Forging. *Mater. Charact.* **2019**, *157*, 109885. [[CrossRef](#)]
78. Kotov, A.D.; Mikhaylovskaya, A.V.; Kishchik, M.S.; Tsarkov, A.A.; Aksenov, S.A.; Portnoy, V.K. Superplasticity of High-Strength Al-Based Alloys Produced by Thermomechanical Treatment. *J. Alloys Compd.* **2016**, *688*, 336–344. [[CrossRef](#)]
79. Mochugovskiy, A.; Kotov, A.; Mikhaylovskaya, A.; Ghayoumabadi, M.E.; Yakovtseva, O. A High-Strain-Rate Superplasticity of the Al-Mg-Si-Zr-Sc Alloy with Ni Addition. *Materials* **2021**, *14*, 2028. [[CrossRef](#)]
80. Kishchik, A.A.; Aksenov, S.A.; Kishchik, M.S.; Demin, D.O.; Churyumov, A.Y.; Mikhailovskaya, A.V. The Microstructure and Mechanical Properties of an Al-Mg-Fe-Ni-Zr-Sc Alloy after Multidirectional Isothermal Forging. *Phys. Met. Metallogr.* **2023**, *124*, 540–549.
81. Yakovtseva, O.; Sitkina, M.; Mosleh, A.O.; Mikhaylovskaya, A. High Strain Rate Superplasticity in Al-Zn-Mg-Based Alloy: Microstructural Design, Deformation Behavior, and Modeling. *Materials* **2020**, *13*, 2098. [[CrossRef](#)]

82. Mikhaylovskaya, A.V.; Esmaili Ghayoumabadi, M.; Mochugovskiy, A.G. Superplasticity and Mechanical Properties of Al–Mg–Si Alloy Doped with Eutectic-Forming Ni and Fe, and Dispersoid-Forming Sc and Zr Elements. *Mater. Sci. Eng. A* **2021**, *817*, 141319. [[CrossRef](#)]
83. Mikhaylovskaya, A.V.; Mochugovskiy, A.G.; Levchenko, V.S.; Tabachkova, N.Y.; Mufalo, W.; Portnoy, V.K. Precipitation Behavior of L1<sub>2</sub> Al<sub>3</sub>Zr Phase in Al–Mg–Zr Alloy. *Mater. Charact.* **2018**, *139*, 30–37. [[CrossRef](#)]
84. Alemdag, Y.; Karabiyik, S.; Mikhaylovskaya, A.V.; Kishchik, M.S.; Purcek, G. Effect of Multi-Directional Hot Forging Process on the Microstructure and Mechanical Properties of Al–Si Based Alloy Containing High Amount of Zn and Cu. *Mater. Sci. Eng. A* **2021**, *803*, 140709. [[CrossRef](#)]
85. Mochugovskiy, A.G.; Mikhaylovskaya, A.V.; Zadorognyy, M.Y.; Golovin, I.S. Effect of Heat Treatment on the Grain Size Control, Superplasticity, Internal Friction, and Mechanical Properties of Zirconium-Bearing Aluminum-Based Alloy. *J. Alloys Compd.* **2021**, *856*, 157455. [[CrossRef](#)]
86. Michi, R.A.; Toinin, J.P.; Seidman, D.N.; Dunand, D.C. Ambient- and Elevated-Temperature Strengthening by Al<sub>3</sub>Zr-Nanoprecipitates and Al<sub>3</sub>Ni-Microfibers in a Cast Al-2.9Ni-0.11Zr-0.02Si-0.005Er (at.%) Alloy. *Mater. Sci. Eng. A* **2019**, *759*, 78–89. [[CrossRef](#)]
87. Suwanpreecha, C.; Toinin, J.P.; Michi, R.A.; Pandee, P.; Dunand, D.C.; Limmaneevichitr, C. Strengthening Mechanisms in Al Ni Sc Alloys Containing Al<sub>3</sub>Ni Microfibers and Al<sub>3</sub>Sc Nanoprecipitates. *Acta Mater.* **2019**, *164*, 334–346. [[CrossRef](#)]
88. Sotoudeh, K.; Bate, P.S. Diffusion Creep and Superplasticity in Aluminium Alloys. *Acta Mater.* **2010**, *58*, 1909–1920. [[CrossRef](#)]
89. Li, H.; Huang, Y.; Liu, Y. Dynamic Recrystallization Mechanisms of As-Forged Al–Zn–Mg–(Cu) Aluminum Alloy during Hot Compression Deformation. *Mater. Sci. Eng. A* **2023**, *878*, 145236. [[CrossRef](#)]

**Disclaimer/Publisher’s Note:** The statements, opinions and data contained in all publications are solely those of the individual author(s) and contributor(s) and not of MDPI and/or the editor(s). MDPI and/or the editor(s) disclaim responsibility for any injury to people or property resulting from any ideas, methods, instructions or products referred to in the content.